Topology and dynamics of the A-pillar vortex

Benjamin Levy[1,2,a)] and Pierre Brancher[1,3]
[1]*Université de Toulouse, INPT, UPS, IMFT (Institut de Mécanique des Fluides de Toulouse), Allée Camille Soula, F-31400 Toulouse, France*
[2]*School of Mechanical Engineering, Shanghai Jiao Tong University, 800 Dongchuan Road, Shanghai 200240, China*
[3]*CNRS, IMFT, F-31400 Toulouse, France*

The topology and dynamics of the flow bypassing an automobile A-pillar modeled by a 30° dihedron are investigated experimentally. The various components of the A-pillar flow are identified by means of low and high frequency particle image velocimetry. For each component, the time evolution of the position, displacement, vorticity magnitude, circulation, and fluctuating kinetic energy are analyzed along the A-pillar. More precisely, the flow bypassing the A-pillar is composed of two vortex structures with different behaviors. The major structure grows in size, circulation magnitude, and total amount of fluctuating kinetic energy along the A-pillar, whereas the minor structure does not vary significantly. Finally, the displacement of the major structure is identified as a movement of precession and the influence of the A-pillar geometry is emphasized.

I. INTRODUCTION

While in motion, a road vehicle generates turbulence, coherent vortical structures, and noise. The corner edge between the windshield and the front side window, known as the A-pillar, is among the most problematic aerodynamic components of a vehicle. The flow bypassing the A-pillar generates an intense three-dimensional coherent structure, the A-pillar vortex, which is not only a localized distribution of vorticity increasing the drag of the vehicle but also a source of intense fluctuations of kinetic energy and wall pressure on the front side window. Nowadays, the A-pillar vortex is also considered as a major source of aeroacoustic noise perceived inside a road vehicle. Therefore, the understanding of its fundamental dynamics is a key element in the long attempt to control and minimize this disturbance.

The oldest public document mentioning some research work on the A-pillar flow is a 90-year-old Dutch patent from the N.V. Instituut voor Aero-En Hydro-Dynamiek.[1] Even though no results are presented, it proves that this research topic is almost as old as the car industry itself. However, it is only in the 1990s that the first scientific researches related to the A-pillar aerodynamics were published with the major exception of Watanabe *et al.*[2] in 1978. They analyzed experimentally the topology of the A-pillar vortex using a simplified geometry of a road vehicle front part represented by a dihedron at 48°. With parietal visualizations, they managed to highlight the existence of two separation lines and one reattachment line, concluding on the existence of two vortices.

The experimental study by Haruna *et al.*[3] on a production vehicle defines a solid basis for the understanding of the phenomenon. They used parietal visualizations to confirm the existence of a region of separation and reattachment on the wall and proposed a plausible explanation for the inner dynamics of the phenomenon.

In 1999, Uchida and Okumura[4] validated the Lattice Boltzmann numerical method as accurately predicting the aerodynamic noise emanating from an A-pillar flow. It led to a series of studies on

a)Electronic mail: benjamin.levy@hotmail.fr.

aeroacoustics[4–6] rather than vortex dynamics due to its concrete industrial application. Meanwhile, the Department of Mechanical and Manufacturing Engineering at the Royal Melbourne Institute of Technology produced a variety of articles on the topic. An experimental comparative study of five models with varying windshield geometries identified the major tendencies of the phenomenon as a function of the angle of attack.[7] Most studies, past and present, do not take into account the presence of the side mirror, for complexity reasons, with the exception of Watkins and Oswald,[8] and Zimmer[9] who quantified its influence on the flow. More precisely, they show that the side mirror creates another vortex structure which slightly impacts the A-pillar flow. Finally, Murad *et al.*[10] compared numerical simulation to past experimental data and concluded that a forward 2nd order $k - \varepsilon$ model was best predicting the flow past an A-pillar, regardless of the angle of attack.

With the recent evolution of the measuring techniques, new approaches of the problem are possible. It is possible to calculate statistic momentums as well as to perform spectral analysis based on experimental data acquired by tridimensional laser velocimetry. With such analysis, it is conceivable to follow the position of the main vortex structure and show that it corresponds to a maximum of fluctuating kinetic energy.[11] Gohlke *et al.*[12] studied how a change in the geometry of the A-pillar radius and the windshield-hood angle could modify the averaged forces applied on a road vehicle under cross-wind. Hoarau *et al.*[13] used laser doppler velocimetry (LDV) and off-set microphones to investigate the wall pressure unsteadiness caused by the A-pillar vortex. They showed that the A-pillar vortex structure could act as a guide for pressure fluctuations and impose the length scale of the perturbations. They concluded on a possible meandering phenomenon for the A-pillar vortex structure.

The present study aims at elucidating the dynamics of the A-pillar flow as it is essential for future studies on side windows pressure fluctuations. Past studies have tried to control the A-pillar vortex but as long as we will not have an accurate understanding of this vortex structure, optimized control methods will be out of reach. Therefore, this study focusses on high resolution results to clarify the different components of the A-pillar flow, through a detailed physical description and the identification of their dynamics.

II. EXPERIMENTAL SETUP

Due to the complexity of the A-pillar flow, we chose to study the flow bypassing a simplified geometry presenting similar characteristics. A dihedron fulfills that purpose. A similar approach was used by Uchida and Okumura[4] for their numerical study of the aerodynamic noise due to the A-pillar vortex. Lehugeur[14] also used a dihedron as a simplified geometry in order to test various control methods of the A-pillar flow, for numerical simulations as well as experiments.[15] Hoarau[13,16] used a slanted dihedron to have a geometry slightly closer to the geometry of a real road vehicle.

From these previous studies, and observations made on real modern road vehicles, a dihedron with a 30° angle was chosen to model a simplified A-pillar. This dihedron was fixed on a back-side front Ahmed body, replacing what used to be the back of the body (Fig. 1). The characteristic length associated to the model, defined as the square root of the apparent cross-section is $L_0 = 0.336$ m.

The wind tunnel used for the experiments is the S1 wind tunnel (Eiffel type) at the Institut de Mécanique des Fluides de Toulouse. It is an open tunnel with an open test section. The diameter

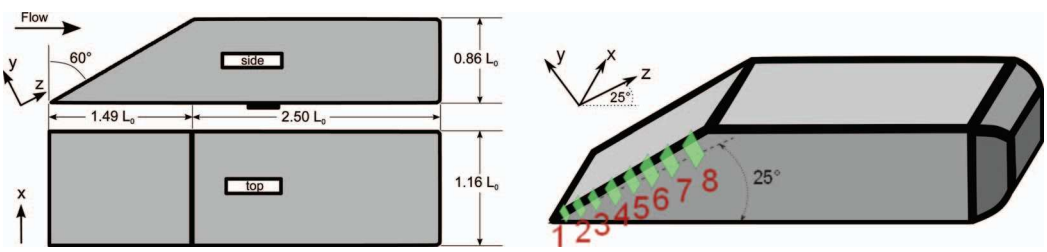

FIG. 1. Geometry and dimensions of the model (left). Position of the eight PIV planes perpendicular to the side wall and perpendicular to the axis of the vortex structures (right). The dashed line corresponds to the axis of the A-pillar vortex at 25° with the horizontal. The PIV planes are in the (x, y) directions and the z-axis is aligned with the A-pillar vortex axis.

of the cross section is 2.4 m. The model was set on a mast at the center of the wind tunnel. The speed of the wind tunnel was set at $U_0 = 8$ m/s. The typical Reynolds number for the experiments is Re $= 170\,000$.

Particle image velocimetry (PIV) at low and high frequency was used for the experimental data acquisition at, respectively, 4 Hz and 1000 Hz. With the help of smoke visualizations, the axis of the A-pillar vortex was identified and observed to be inclined at an angle of 25° with the horizontal axis. Therefore, the camera was set behind the model with a 25° angle with the horizontal axis. Thus it was possible to obtain cross sections of the vortex at different locations along the A-pillar. On the whole, eight different sets of acquisitions were performed (Fig. 1) at distances from the front of the model along the A-pillar of, respectively, 0.38 L_0, 0.53 L_0, 0.68 L_0, 0.82 L_0, 0.96 L_0, 1.10 L_0, 1.25 L_0, 1.54 L_0. The material used for the low frequency PIV was a Quantel Laser CFR 200 with 2 × 200 mJ cavities at a frequency of 4 Hz and a Sensicam camera with a resolution of 1280 × 1024 pixels mounted with a Nikon lens (55–160 mm). For the high frequency experiments, a Darwin Duo 2 × 20 mJ from Quantronix and a photron APX with a resolution of 1024 × 1024 pixels and a 135 mm Nikon lens were used. Di(2-ethylhexyl)sebacate (DEHS) was used as a seeding with particles of diameter 0.5–1.5 μm and a time response of about 25 μs.[17] The flow was analyzed by cross-correlating 50% overlapping windows of 16 × 16 pixels, yielding fields of 160 × 128 or 128 × 128 vectors with a spatial resolution of 0.312 mm (0.00092 L_0), 0.392 mm (0.00117 L_0), 0.664 mm (0.00198 L_0), and 0.816 mm (0.00243 L_0), respectively, for plane 1, planes 2–3, planes 4–5, and planes 6–8. Less than 2% of the calculated vectors were detected as outliers using a sort based on the norm, the signal-to-noise ratio, and a median test filter. These vectors were replaced using a second order least square interpolation scheme. There is a 2.4% uncertainty on the data.

From the analysis of the velocity divergence in each PIV plane, it is possible to validate the approximation of a two-dimensional flow within the planes 1–8 (Fig. 2). For an incompressible flow, the divergence is defined by

$$\mathrm{div}\mathbf{u} = \frac{\partial u}{\partial x} + \frac{\partial v}{\partial y} + \frac{\partial w}{\partial z} = 0 \tag{1}$$

meaning that, from the two-dimensional PIV data (u, v), it is possible to have access to the velocity variations in the third direction $\partial w/\partial z$. Figure 2 displays these averaged data for three different planes. The spatial fluctuations are not significant and are related to acquisition noises as the spatial repartition of $\partial w/\partial z$ is too random to correspond to the projection in the (x, y) plane of a coherent vortex structure. It is then possible to conclude that $\partial w/\partial z$ is negligible and that the flow is locally quasi two dimensional.

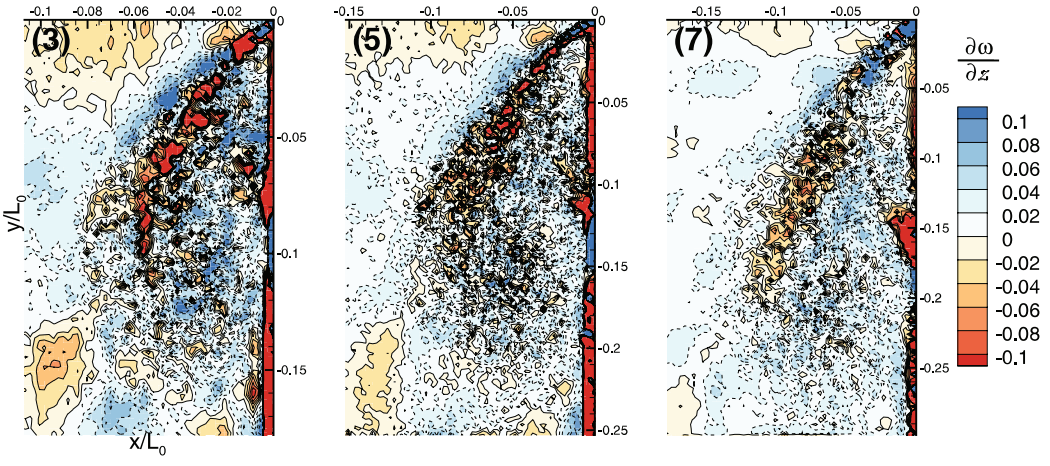

FIG. 2. Representation of $\partial w/\partial z$ for the plane 3, 5, and 7 showing the validity of the bidimensional approximation (solid lines for positive values and dashed lines for negative values).

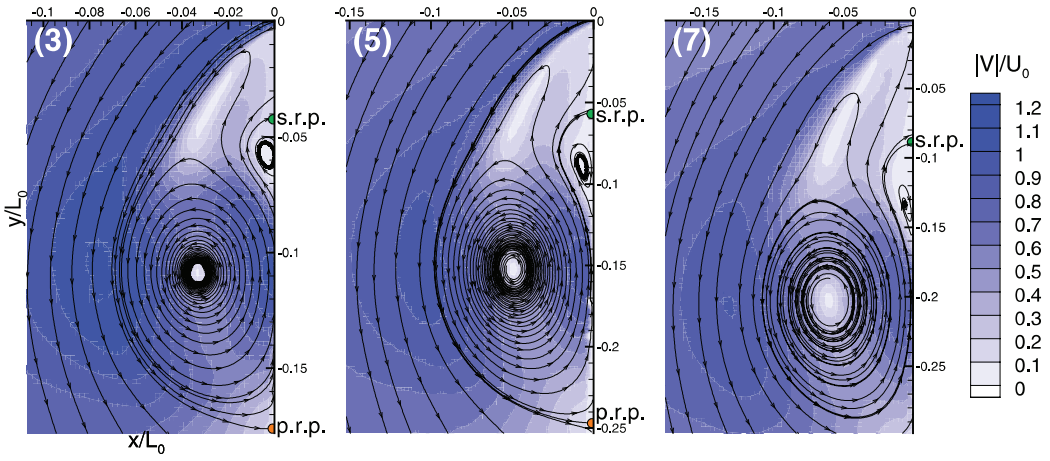

FIG. 3. Normalized velocity module for planes 3, 5, and 7, with indication of the location of the primary reattachment point (p.r.p.) and of the secondary reattachment point (s.r.p.).

By analyzing multiple cross sections of the phenomenon along the corner edge of the A-pillar, it is possible to extract from two-dimensional data a representation of its spatial evolution from the bottom to the top of the A-pillar.

III. ANALYSIS OF THE MEAN FLOW

Figure 3 displays the module of the velocity field normalized by the upstream velocity U_0 and the corresponding sectional streamlines. This gives an overview of the topology of the A-pillar vortex structures.

From previous works and the upcoming results of the present study, the following topology nomenclature was chosen to define the different features of the A-pillar flow: primary vortex, secondary vortex, primary and secondary reattachment point, primary and secondary separation point, mixing or shear layer, inner separatrix and outer separatrix (Fig. 4), the physics of which will be detailed in Sec. III.

From this information, it is possible to follow the evolution of the mean position of the vortex structures in the different (x, y) planes along the A-pillar as well as the phenomenon geometry

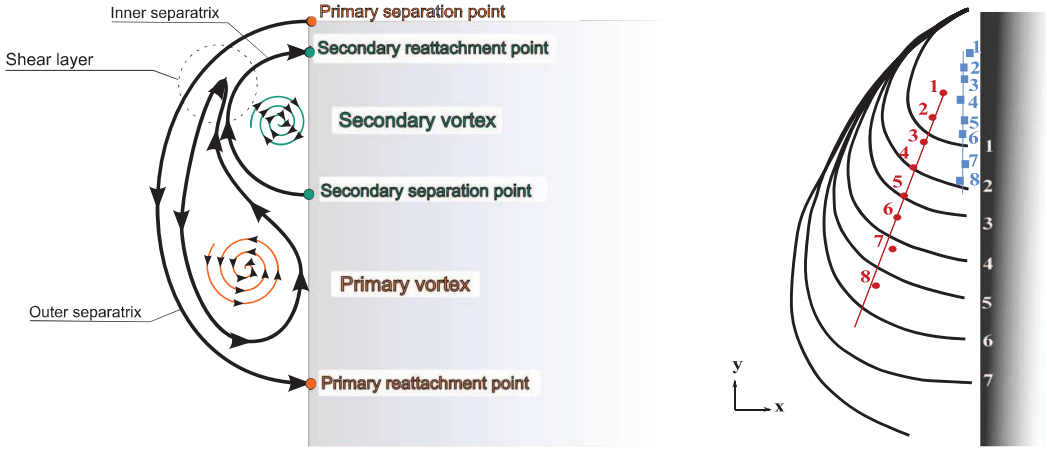

FIG. 4. Nomenclature of the flow bypassing the A-pillar (as observed in PIV planes, left). Evolution of the size of the outer separatrix in the planes 1–8 along the A-pillar (right), and spatial evolution of the center of the primary vortex (red dots) and of the secondary vortex (blue squares).

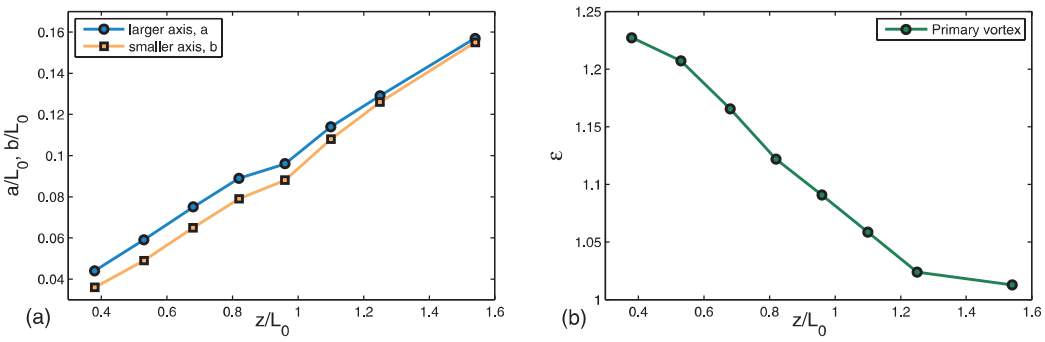

FIG. 5. (a) Evolution of the major axis a and the minor axis b (in mm) of the primary vortex structure along the A-pillar. (b) Evolution of the aspect ratio $\varepsilon = a/b$ of the primary vortex structure along the A-pillar.

defined by the outer separatrix (Fig. 4). There are three major observations to be made. The shape of the phenomenon stays qualitatively the same and only increases in size; the mean center of the primary vortex moves away linearly from the wall; the mean center of the secondary vortex evolves along a trajectory almost parallel to the wall.

Let ε define the aspect ratio of a cross section of the phenomenon or one vortex structure:

$$\varepsilon = \frac{a}{b}, \tag{2}$$

where a denotes the major axis and b the minor axis. For the primary vortex structure, it is observed that the major axis and the minor axis defined using the Q criterion (see Eq. (3)), are linearly increasing (Fig. 5(a)) and that the aspect ratio converges towards 1 (Fig. 5(b)). This means that the primary vortex structure tends to become circular. It is possible to estimate the aspect ratio of the phenomenon envelope, defined by the outer separatrix, meaning a is defined as the distance between the primary separation and reattachment point (Fig. 4) and b as the maximum distance between the wall and the outer separatrix. It is shown that the envelope of the phenomenon is very elliptic, with a quasi constant aspect ratio $\varepsilon \sim 2.5$. It is a radically different tendency than the one observed for the primary vortex structure.

A careful analysis of the streamlines allows the reattachment point mentioned in previous numerical studies[4,6,18] to be well identified (Fig. 3), as well as the separation point that is not always mentioned in numerical simulations. On the upstream part of the model (planes 1–3), the free flow bypassing the A-pillar vortex is accelerated by up to 20% despite undergoing a change of orientation (Fig. 6). There is a 25° angle between the upstream flow and the planes within which it is recorded through PIV.

Symmetrically to the center of the primary vortex structure, a second area of important acceleration can be observed near the wall with speeds up to $1.07U_0$. As the vortex structure develops itself along the A-pillar, the velocities inside the outer separatrix considerably decrease. Within the area defined previously as the shear layer and the one within the inner separatrix, the flow almost comes to a still stand since the velocity magnitude is as low as $0.1U_0$ at the level of the 8th plane (Figs. 3 and 6).

In order to highlight the observed structures and precisely define their outer limits, the Q criterion as defined by Jeong and Hussain[19] can be applied (Fig. 7):

$$Q = \frac{1}{2}\left(||\mathbf{\Omega}||^2 - ||\mathbf{S}||^2\right) = -\frac{\partial v}{\partial x}\frac{\partial u}{\partial y} - \frac{1}{2}\left[\left(\frac{\partial u}{\partial x}\right)^2 + \left(\frac{\partial v}{\partial y}\right)^2\right] \geqslant 0, \tag{3}$$

where $\mathbf{\Omega}$ and $\mathbf{S}$ are, respectively, the symmetric and antisymmetric parts of the velocity gradient tensor. $Q \geq 0$ defines the region where rotation is larger then deformation and is therefore used to identify vortices.

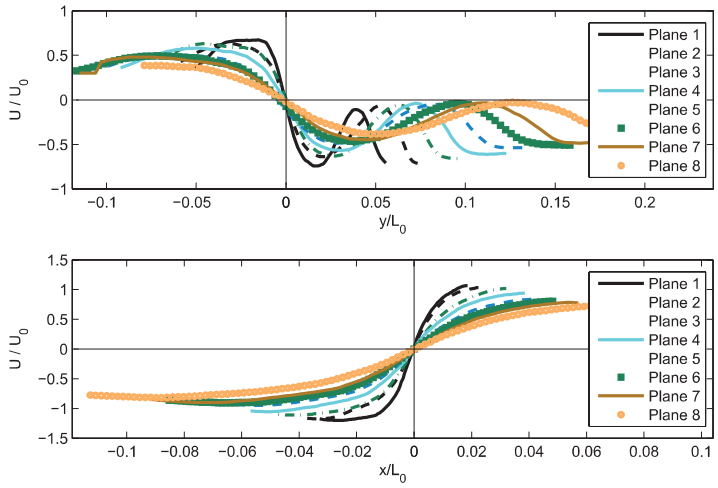

FIG. 6. Velocity profiles along x and y normalized by U_0, with origin at the center of the primary vortex structure for the planes 1–8.

The Q criterion confirms the existence of the two distinct vortex structures: the *primary vortex* as the largest structure and the *secondary vortex* as a smaller structure located in the region of recirculation defined previously. A third structure located above the secondary vortex might exist at the level of the plane 1 (data not shown). Whenever it was the case, it was observed to vanish within the shear layer generated by the bypassing flow. The Q criterion also highlights the region of important shear, located between the two vortices as well as a second shear layer of lower magnitude near the primary reattachment point (Fig. 7).

The study of the vorticity field (Fig. 8) confirms the observations made previously: there are two vortical structures of opposite sign. However, it is noteworthy that the vorticity does not show evidence of a third vortex structure within the shear layer in plane 1 (data not shown).

The spatial development of the vortex structures along the edge and their decrease in intensity points out the diffusion of vorticity along the A-pillar. Vorticity profiles along the x or y axis with origin at the center of the primary vortex, allow a better quantification of this observation (Fig. 9). The dissipation rate at the center of the vortex is equivalent to the one in the shear layer from the second plane of observation on, its tendency is $\omega \sim z^{-1.38}$. Even though the vorticity magnitude maximum within the primary vortex decreases, the circulation Γ (Eq. (4)) of the primary vortex

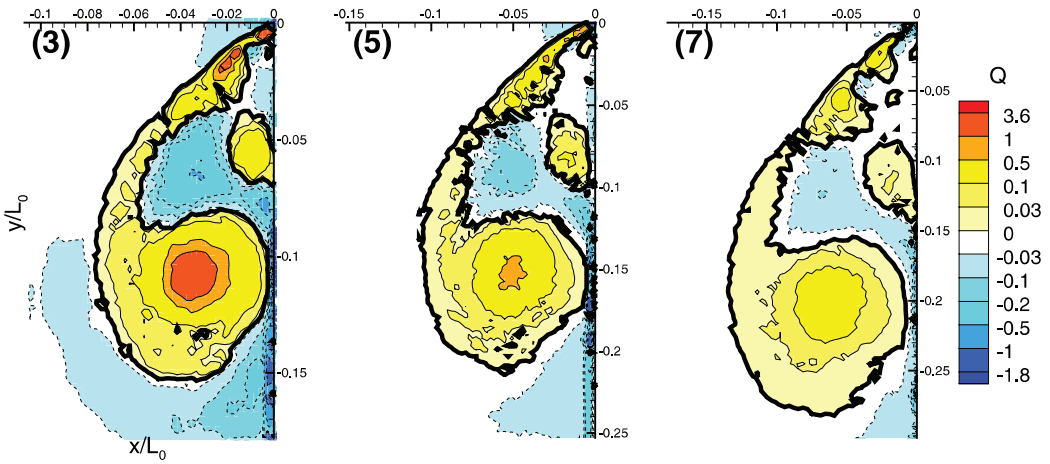

FIG. 7. Q criterion in planes 3, 5, and 7. Solid contour lines for positive values and dashed contour lines for negative values. The contour $Q = 0$ is displayed as a bold line.

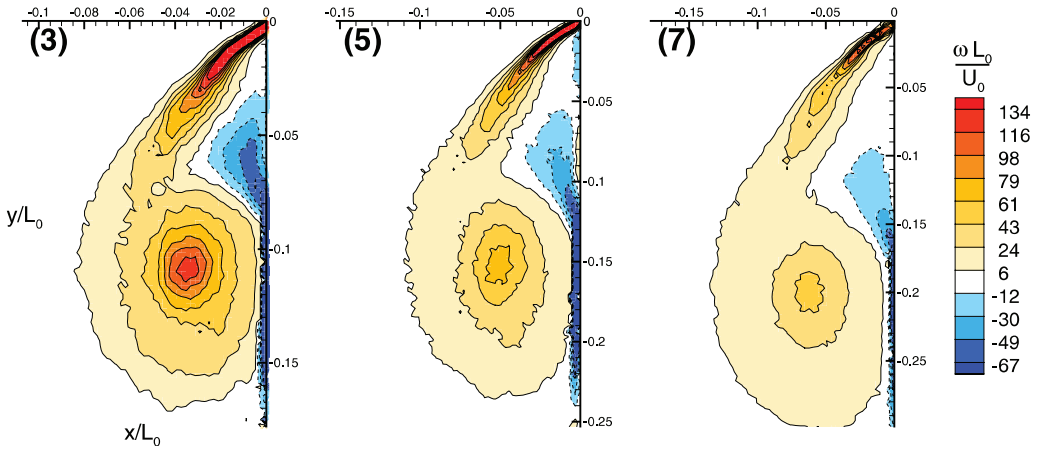

FIG. 8. Normalized (out-of-plane) vorticity field in the planes 3, 5, and 7. Solid contour lines for positive values and dashed contour lines for negative values.

increases up to twice its initial value (Fig. 10). This could be due to a permanent supply all along the A-pillar of the boundary layer vorticity coming from the windshield. It should be noted that the circulation

$$\Gamma = \int \omega dS \tag{4}$$

is calculated using $Q = 0$ as the limit of integration. Though objective, this choice leads the shear layer to be integrated as well (Fig. 7). Therefore, the value of the circulation obtained that way is overestimated (solid line in Fig. 10). A second estimation for the circulation was made by subtracting the circulation of the mixing layer. The downside is that the limitation between those two areas is not well defined and it is most likely that a small part of the primary vortex structure is being left out by this process. This second method slightly underestimates the circulation of the primary vortex (dotted line on Fig. 10) but the values differ only by 7% from the first method. Those two approaches give a range within which the exact value of the circulation of the primary vortex is expected. They both have a very similar growth in z.

The intensity of the vorticity within the secondary vortex decreases as the phenomenon develops itself along the A-pillar (Fig. 8). Nevertheless, the circulation of the secondary vortex is quasi constant

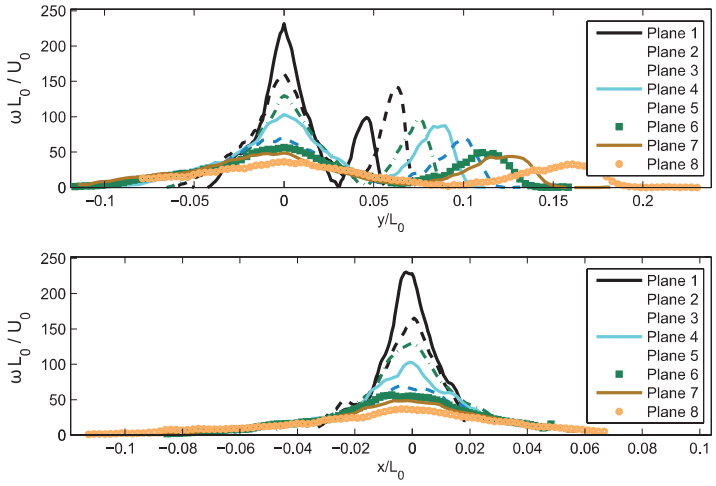

FIG. 9. Vorticity profiles along x and y, with origin at the center of the primary vortex structure, for the planes 1–8.

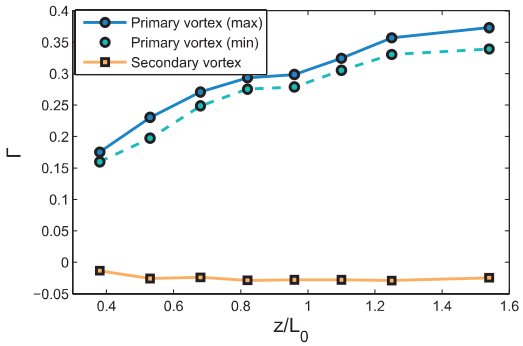

FIG. 10. Evolution of the circulation of the primary vortex (Eq. (4)) calculated within the whole $Q > 0$ region (max) and outside the shear layer (min). See text for details. Also displayed is the circulation of the secondary vortex along the A-pillar.

from planes 2 to 8 (Fig. 10). It means that there is only a reorganization of the vorticity within this vortex structure.

IV. ANALYSIS OF THE FLUCTUATIONS

A. Low-frequency particles image velocimetry

The fluctuating kinetic energy E'_k gives access to the regions of significant unsteadiness (Fig. 11).

Three regions of significant fluctuating kinetic energy are identified. One is the center of the primary vortex, which means that it moves a lot around its averaged position. A second region coincides with the shear layer. And the third region corresponds to the secondary separation point, located between the primary and the secondary vortex structures, which suggests that its position on the wall fluctuates.

As previously, it is possible to get a better quantification of these observations by looking at profiles along x and y (Fig. 12). It is found that E'_k at the center of the primary vortex decreases by 57%. The local maximum values of fluctuating kinetic energy in the primary vortex, in the shear layer and next to the secondary separation point decrease along the A-pillar (Fig. 13(a)). It is noticeable that the decay rate is very similar at these three different locations, with $E'_{k_{max}} \sim z^{-7/11}$.

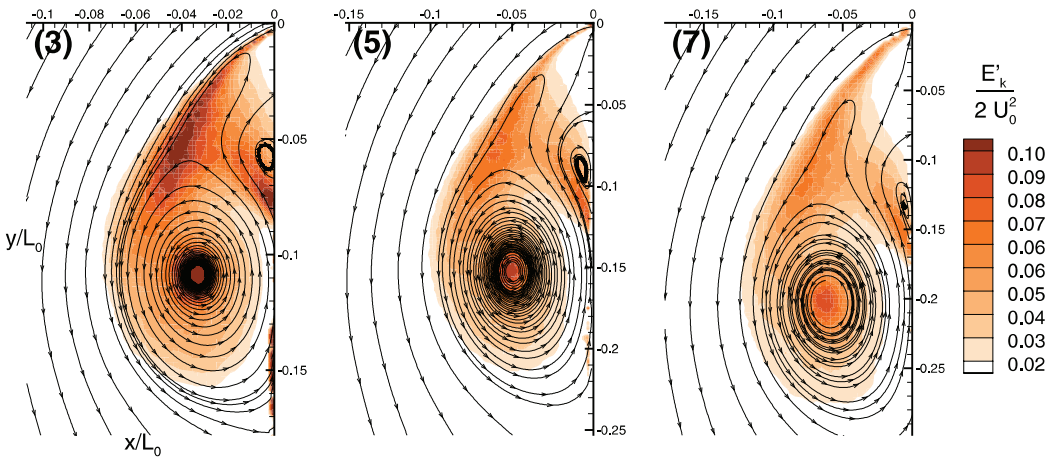

FIG. 11. Normalized fluctuating kinetic energy field in planes 3, 5, and 7.

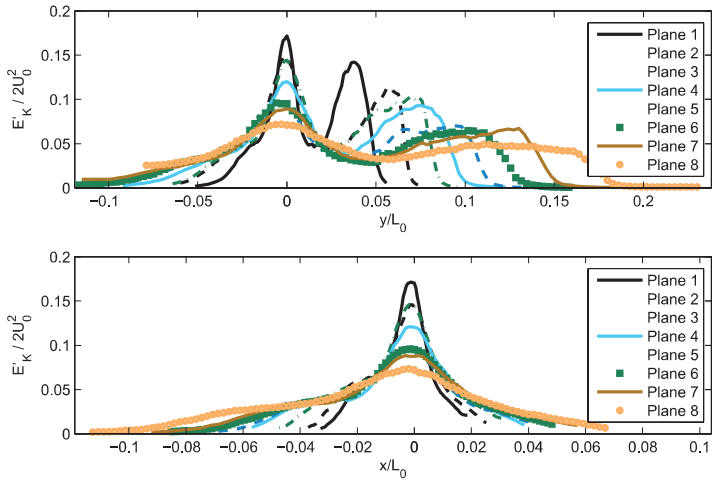

FIG. 12. Profiles of fluctuating kinetic energy along x and y, with origin on the center of the primary vortex structure, in planes 1–8.

A total integrated fluctuating kinetic energy can be measured in a similar manner as the circulation:

$$E'_{total} = \int E'_k dS. \tag{5}$$

For the primary vortex, E'_{total} grows linearly and increases by a factor 6 between the first and the last planes as the vortex evolves along the A-pillar (Fig. 13(b)). This result shows that the A-pillar vortex accumulates more fluctuating energy than it dissipates as it grows along the A-pillar.

B. High-frequency particles image velocimetry

In order to get a better understanding of the dynamics controlling the A-pillar vortices, the use of high frequency PIV is required. The raw data are however contaminated by some significant noise originating from small erratic perturbations. In order to study the dynamics of the A-pillar bypassing flow, it is necessary to be able to identify precisely the center of the two vortex structures. For that purpose, proper orthogonal decomposition (POD) can be applied, based on the method first introduced by Lumley[20] and then developed into the snapshots method by Sirovich.[21–23]

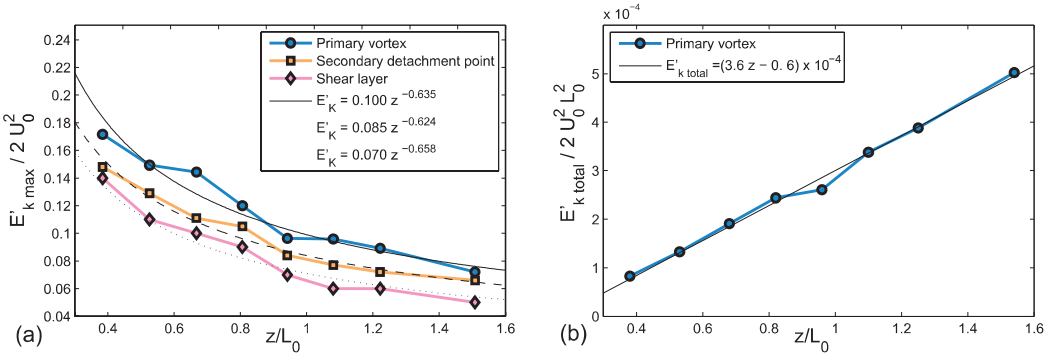

FIG. 13. (a) Evolution of the maximum fluctuating kinetic energy at the center of the primary vortex, at the secondary separation point, and in the shear layer, with best fits displayed, respectively, in solid, dashed, and dotted lines. (b) Evolution of the total amount of fluctuating kinetic energy within the primary vortex and associated linear regression curve.

Let us define

$$A = \begin{pmatrix} A_1 & \dots & A_{N_t} \end{pmatrix}; A_i = \begin{pmatrix} u'_{1,i} \\ \vdots \\ u'_{N,i} \\ v'_{1,i} \\ \vdots \\ v'_{N,i} \end{pmatrix}, \tag{6}$$

where N_t is the number of observations (or "snapshots"). Then the eigenvalues λ_k and the eigenvectors $V_{\lambda k}$ associated to the correlation matrix

$$C = A^T A \tag{7}$$

are computed and replaced in the following Eqs. (8) and (9) that define the orthonormal modes $\phi_k(x)$ and the time dependent functions $a_k(t)$:

$$\phi_k = \frac{1}{\sqrt{\lambda_k}} A V_{\lambda_k}, \tag{8}$$

$$a_k = A^T \phi_k = \frac{V_{\lambda_k}}{\sqrt{\lambda_k}}. \tag{9}$$

It is then possible to compute

$$U(x,t) \simeq U_m(x) + \sum_{k=1}^{N} a_k(t)\phi_k(x), \tag{10}$$

where $U(x, t)$ is the recomposed flow made of the time averaged flow $U_m(x)$ and the sum of the first N most energetic modes dominating the flow dynamics. For further details regarding the POD, the reader can refer to Cordier and Bergmann.[24]

The relative statistical content of the truncated POD basis as a function of the mode number (I_{Npod}) has a slow growth (Fig. 14). Even though the first six modes are representing only 37% of the statistical content, they are sufficient to extract the primary and secondary vortex structure from the surrounding noise (Eq. (10) with N = 6). If more modes are used for the reconstruction of the flow, no further statistical content regarding the major dynamics of the structures is added and only small-scale noise emerges, making the identification of the vortex centers more difficult. Anyway, the variations of the vortex positions are well represented by the first few POD modes as the higher modes are more related to the deformation of the structure and the small-scale fluctuations of the

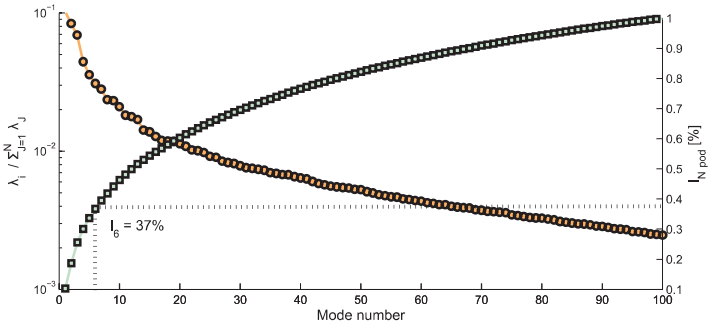

FIG. 14. Relative statistical content of each POD mode (orange circles) and relative statistical content of the truncated POD basis as a function of the mode number (green squares).

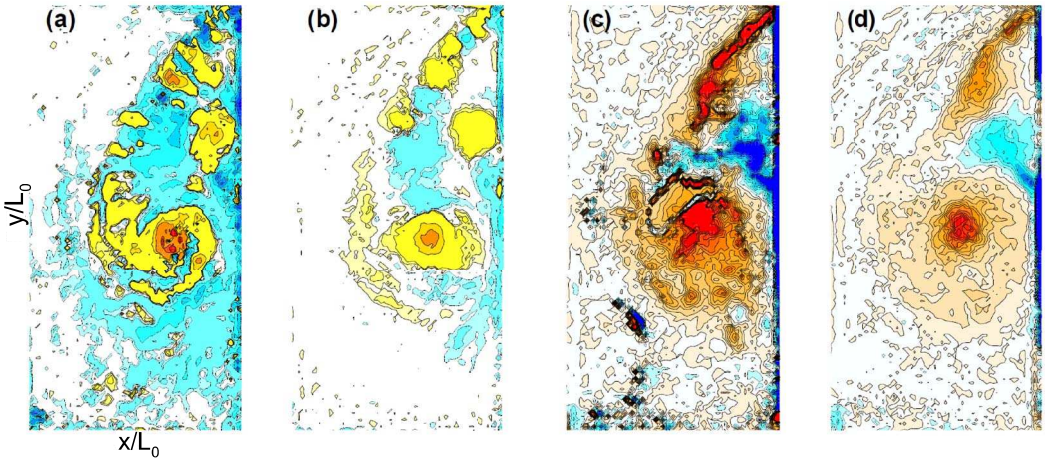

FIG. 15. Instantaneous fields of the Q criterion (a) without POD filtering, (b) with a 6 POD mode filtering. Instantaneous fields of vorticity ω (a) without POD filtering and (b) with 6 POD mode filtering.

flow. Figure 15 shows a comparison of instantaneous fields of the Q criterion (without POD filtering and with a 6 POD modes filtering) and instantaneous vorticity fields ω (without POD filtering and with a 6 POD modes filtering). These results suggest that this level of truncation is reasonable.

It is then possible to track the trajectory of the vortex structures in time. Because of its size and its high fluctuating kinetic energy, the primary vortex is the main actor of the flow dynamics and therefore the one we focused on. The raw data were first filtered using the POD decomposition (Eq. (10)). For each snapshot, the theoretical center of the vortex structure is identified. For this purpose, a barycentric calculation based on the vorticity or the Q criterion can be performed. To overcome problems related to the geometry of the structure, the computational domain has been defined by $Q \geq 0.5$. The results obtained with the vorticity being almost identical to the one obtained with the Q criterion, only the later are being used in the following.

By proceeding to a space-time tracking of the primary vortex center in the (x, y) plane, no well-defined trajectory is identifiable but rather an erratic motion within a restricted, well defined, area (Fig. 16). With the use of a coarse computational mesh, the very small perturbations can be

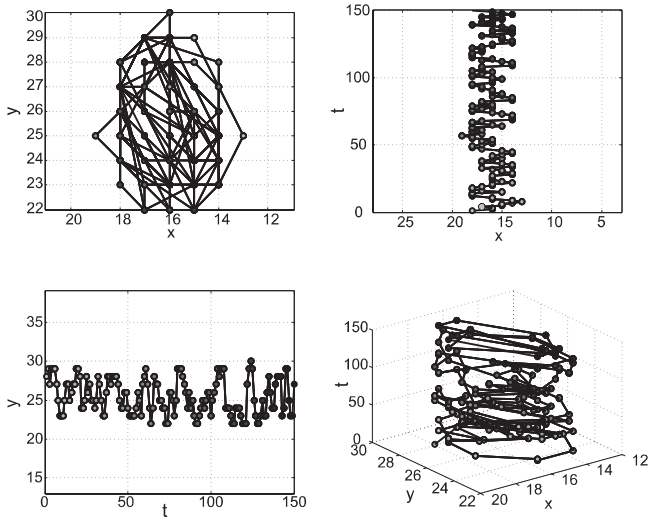

FIG. 16. Temporal tracking of the primary vortex center displacement measured in plane 7 for a sample of 150 timesteps in the (x, y), (x, t), and (t, y) planes, and (x, y, t) space. Here x, y, and t correspond, respectively, to grid nodes and time iterations, associated to the space and time discretization.

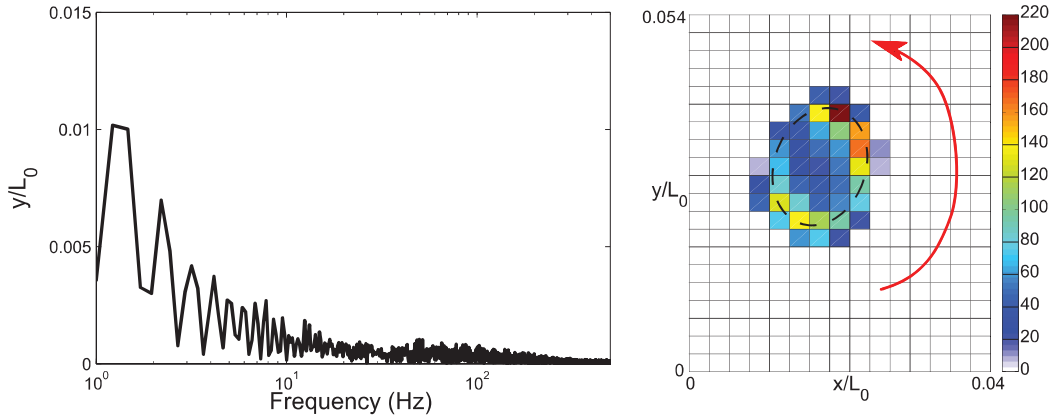

FIG. 17. Frequency spectrum (left) of the primary vortex center displacements in the y-direction obtained by Fourier analysis (based on the Q criterion). Location density probability (right) of the primary vortex center for 3000 consecutive snapshots. The dashed line highlights the movement of precession made by the primary vortex core and the red arrow the main direction of rotation.

filtered out. It becomes possible to compare the evolution of the position of the vortex core for two consecutive snapshots compared to its averaged position. It turns out that the primary vortex has a preferred direction of rotation which is counterclockwise for 70% of the time (Fig. 17).

A fast Fourier transform of the primary vortex center displacement over time displays a frequency spectrum without any clear frequency peak. It is shown that the phenomenon is associated to low frequencies, between 1.2 Hz and 1.5 Hz (Fig. 17). These frequencies correspond to a Strouhal number $St = fL_0/U_0$ between 0.05 and 0.06.

The analysis of the location density probability for the center of the primary vortex (Fig. 17) reveals that the averaged position does not correspond to the positions with the highest density. The later is located on the edge of the region around which the vortex center moves. The positions with the highest densities are all located on the outer edge of the elliptic area within which the primary vortex core moves. This result suggests that the vortex core has a movement of precession.

V. INFLUENCE OF THE GEOMETRY

The phenomenon observed and described previously depends a lot on the geometry of the model and more particularly on the geometry of the corner edge. In order to emphasize the importance of

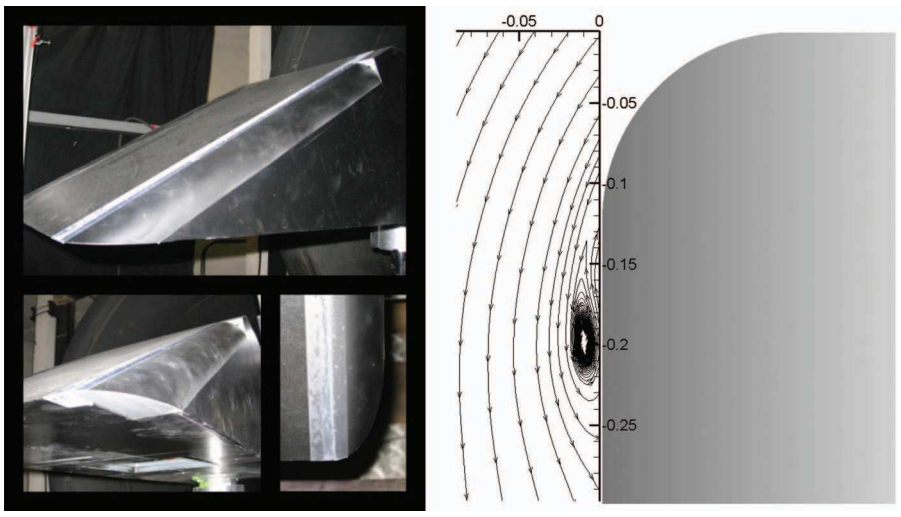

FIG. 18. Rounded A-pillar with a radius of 40 mm. Streamlines of the mean flow in plane 7 obtained by PIV.

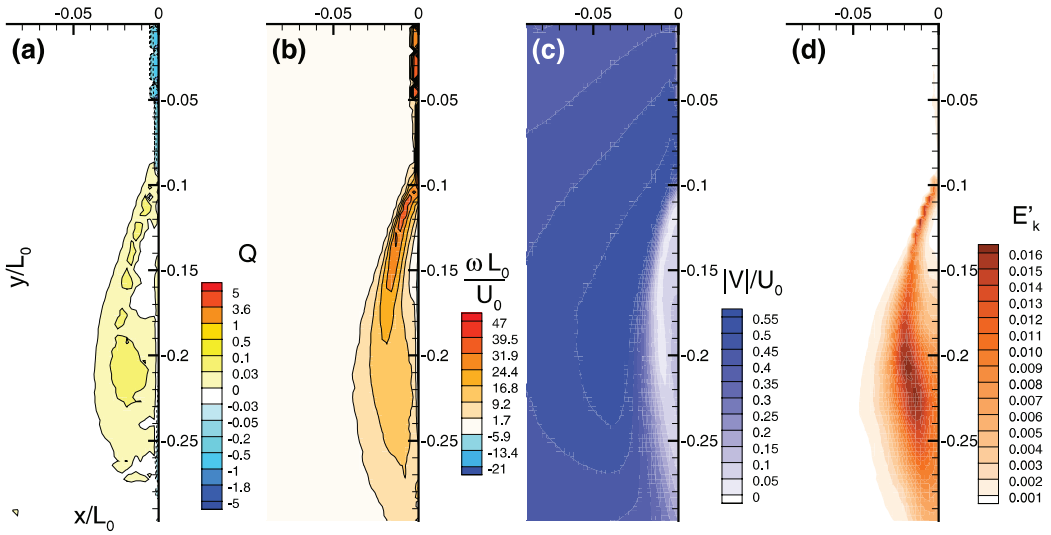

FIG. 19. Analysis of the mean flow bypassing the rounded A-pillar: (a) Q criterion; (b) normalized vorticity ω; (c) normalized velocity module; (d) fluctuating kinetic energy E'_k (negative values with dashed contour lines).

the geometry in the formation of the A-pillar vortex structures, the right angle edge was replaced by a rounded edge with a radius of curvature of 40 mm, presenting no discontinuities with either side of the model (Fig. 18).

As previously, the new flow topology and dynamics can be analyzed using high frequency PIV. Only plane 7 is discussed as it is sufficient to emphasize the differences between the previous flow and the new flow obtained with the rounded edge. Looking at the time averaged Q criterion, vorticity ω, normalized velocity module, fluctuating kinetic energy E'_k (Fig. 19), and streamlines (Fig. 18), the first observation is that the flow is completely modified compared to the previous one. The new A-pillar bubble is much smaller: -74% in the x direction and -33% in the y direction corresponding to an aspect ratio much greater, of 9.6 instead of 2.5.

The analysis of the Q criterion and the vorticity field shows that the primary and secondary vortices observed in the previous case are no longer visible. The vorticity magnitude is very low compared to the previous flow, and there is no negative vorticity. Near the wall, the flow drastically slows down to $0.1U_0$. That explains why, with a 30° yaw-angle, Gohlke *et al.*[12] observed a much smaller and closer to the surface vortex structure at the rear lee-side of a modeled road vehicle.

With the instantaneous data, it is possible to follow the temporal evolution of the vorticity at any point in plane 7 (Fig. 20), as was previously done for the right angle A-pillar (Fig. 17). A FFT of the recorded signal at ($x = -6$, $y = -80$) shows a weak periodical phenomenon associated to the flow bypassing the circular A-pillar, at a frequency of about $f = 50$ Hz or $St = fL_0/U_0 = 2.1$. The existence of a periodic feature in the flow dynamics is confirmed by the POD modes representation

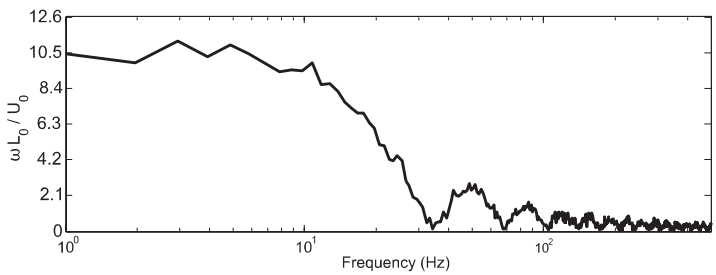

FIG. 20. Fast Fourier transform of the vorticity magnitude temporal evolution within the area of perturbation past the rounded A-pillar.

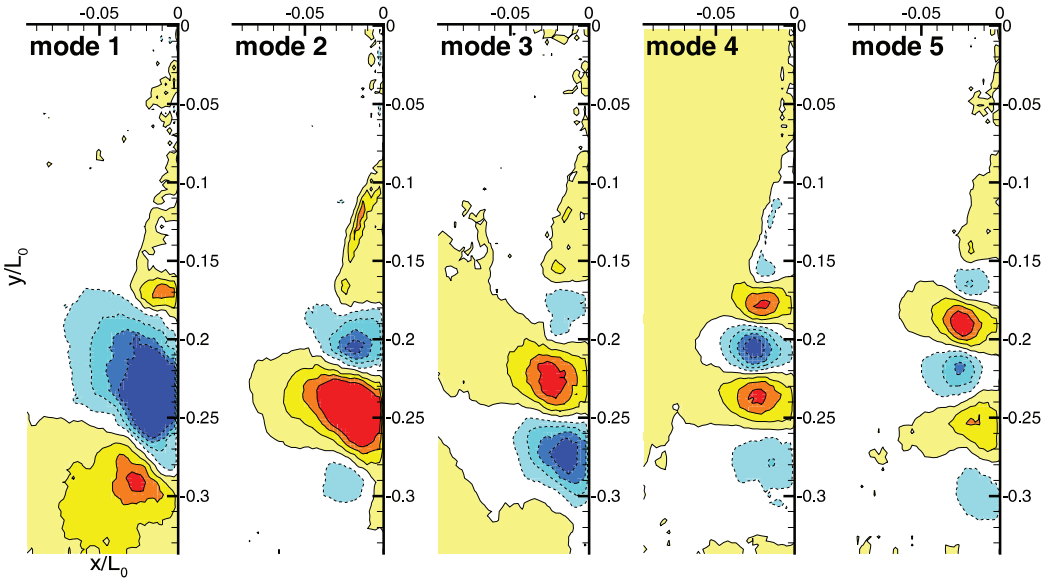

FIG. 21. First 5 POD modes associated to the U_y velocity component (negative contours in dotted lines).

based on U_y, which are characteristics of a shear layer in the presence of regular vortex structures being convected downstream, similar to the vortices generated by the Kelvin-Helmholtz instability of the shear layer (Fig. 21).

VI. CONCLUSION

The use of low and high frequency PIV has shown in the case of a right angle A-pillar that the envelope of the A-pillar vortex phenomenon has an elliptic shape and is made of a primary vortex and a secondary, counter-rotating, vortex of lower intensity and dimensions. The center of the primary vortex moves away from the wall as it develops along the edge of the A-pillar while the secondary vortex remains near the wall, both with linear trajectories. The separation point, the center of the primary vortex, and the shear layer are the regions of highest fluctuating kinetic energy and their intensities decrease as $E'_{k_{max}} \sim z^{-7/11}$, whereas the total fluctuating kinetic energy increases linearly. Moreover, despite a decay of the maximum vorticity magnitude within the primary vortex structure, the circulation Γ increases in z.

The study of the flow based on high frequency PIV has highlighted the displacement dynamics of the primary vortex. It exhibits a low frequency response (1–2 Hz) associated to very low Strouhal numbers, but its oscillations are mostly erratic. Moreover, it is found that the vortex center has a movement of precession which is mostly counterclockwise around its time-averaged position.

Finally, the influence of the A-pillar geometry on the structure of the flow has been confirmed by replacing the initial sharp A-pillar by a rounded edge. The topology of the new flow fundamentally differs from the previous one. There is no dominant vortex structures and the dynamics of the flow is very similar to that of a shear layer subjected to Kelvin-Helmholtz instabilities.

[1] E. Bert, Technical Report 586.613, N.V. Instituut voor Aero-En Hydro-Dynamiek, 1925.
[2] M. Watanabe, M. Harita, and E. Hayashi, "The effect of body shapes on wind noise," SAE Technical Paper 780266 (1978).
[3] S. Haruna, T. Nouzawa, and I. Kamimoto, "An experimental analysis and estimation of aerodynamic noise using a production vehicle," SAE Trans. 667 (1990).
[4] K. Uchida and K. Okumura, "Aerodynamic noise simulation based on Lattice Boltzmann Method (surface pressure fluctuations around A-pillar)," SAE Technical Paper 1999-01-1127 (1999).
[5] O. Vaillant and V. Maillard, "Numerical simulation of wall pressure fluctuations on a simplified vehicle shape," in *9th AIAA/CEAS Aeroacoustics Conference and Exhibit* (ASME, 2003), Vol. 115.
[6] A. Gaylard, "CFD simulation of side glass surface noise spectra for a bluff SUV," SAE Technical Paper 2006-01-0137 (2006).

[7] F. Alam, S. Watkins, and G. Zimmer, "Mean and time-varying flow measurements on the surface of a family of idealised road vehicles," Exp. Therm. Fluid Sci. **27**, 639 (2003).
[8] S. Watkins and G. Oswald, "The flow field of automobile add-ons with particular reference to the vibration of external mirrors," J. Wind Eng. Ind. Aerodyn. **83**, 541 (1999).
[9] G. Zimmer, "A study of passenger car A-pillar vortex effects using different experimental methods," Ph.D. dissertation, RMIT University, 2004.
[10] N. Murad, J. Naser, F. Alam, and S. Watkins, "Simulation of vehicle A-pillar aerodynamics using various turbulence models," SAE Technical Paper 2004-01-0231 (2004).
[11] M. Gohlke, J. Beaudoin, M. Amielh, and F. Anselmet, "Effect of unsteady separation on an automotive bluff-body in cross-wind," in *IUTAM Symposium on Unsteady Separated Flows and their Control* (Springer Netherlands, 2009), Vol. 14, p. 35.
[12] M. Gohlke, J. Beaudoin, M. Amielh, and F. Anselmet, "Shape influence on mean forces applied on a ground vehicle under steady cross-wind," J. Wind Eng. Ind. Aerodyn. **98**, 386 (2010).
[13] C. Hoarau, J. Borée, J. Laumonier, and Y. Gervais, "Unsteady wall pressure field of a model A-pillar conical vortex," Int. J. Heat Fluid Flow **29**, 812 (2008).
[14] B. Lehugeur, "Caractérisation et contrôle des structures tourbillonnaires longitudinales en aérodynamique automobile," Ph.D. dissertation, Université Pierre et Marie Curie, 2007.
[15] B. Lehugeur and P. Gilliéron, "Active control of vortex breakdown phenomenon in the wake of a simplified car geometry," ASME Conf. Proc. **2006**, 709.
[16] C. Hoarau, "Mesures multipoints pression - vitesse pour l'analyse de l'aérodynamique d'écoulements décollés instationnaire - Application aux véhicules terrestres," Ph.D. dissertation, Université de Poitiers, 2006.
[17] M. Raffel, C. E. Willert, S. T. Wereley, and J. Kompenhans, *Particle Image Velocimetry—A Practical Guide* (Springer, 2007).
[18] K. Ono, R. Himeno, and T. Fukushima, "Prediction of wind noise radiated from passenger cars and its evaluation based on auralization," J. Wind Eng. Ind. Aerodyn. **81**, 403 (1999).
[19] J. Jeong and F. Hussain, "On the identification of a vortex," J. Fluid Mech. **285**, 69 (1995).
[20] J. Lumley, "The structure of inhomogeneous turbulence," in *Atmospheric Turbulence and Wave Propagation*, edited by A. M. Yaglom and V. I. Tatarski (Nauka, Moscow, 1967), p. 166.
[21] L. Sirovich, "Turbulence and the dynamics of coherent structures. Part 1: Coherent structures," Q. Appl. Math. **XLV**(3), 561 (1987).
[22] L. Sirovich, "Turbulence and the dynamics of coherent structures. Part 2: Symmetries and transformations," Q. Appl. Math. **XLV**(3), 573 (1987).
[23] L. Sirovich, "Turbulence and the dynamics of coherent structures. Part 3: Dynamics and scaling," Q. Appl. Math. **XLV**(3), 583 (1987).
[24] L. Cordier and M. Bergmann, "Proper orthogonal decomposition: an overview," in *Post-Processing of Experimental and Numerical Data*, VKI Lecture Series 2003-03, edited by P. Millan and M. L. Riethmuller (Von Karman Institute for Fluid Dynamics, 2003).